Computation of Mass Transport Properties of Apple and Rice from X-ray Microtomography Images

Alexander Warning[1], Pieter Verboven[2], Bart Nicolaï[2,4], Gerard-Van Dalen[3], Ashim K Datta[1]

[1]Department of Biological and Environmental Engineering, Cornell University, 208 Riley-Robb Ithaca, NY, 14853-5701 USA.

[2]BIOSYST-MeBioS, KU Leuven, Willem de Croylaan 42 - box 2428, 3001 Leuven, Belgium

[3]Advanced Measurement and Data Modeling, UnileverR&D Olivier van Noortlaan 120, 3133AT Vlaardingen, the Netherlands

[4]VCBT, Flanders Centre of Postharvest Technology, Willem de Croylaan 42 - box 2428, 3001 Leuven, Belgium

Corresponding Author: Ashim K Datta, Department of Biological and Environmental Engineering, Cornell University, 208 Riley-Robb Ithaca, NY, 14853-5701 USA.

Email: akd1@cornell.edu

Telephone: 607-255-2482

Abstract

Computational simulations of food processes such as baking, frying, and cooling require transport properties in order to accurately model the process. Coupled with the increased usage of X-ray computed microtomography to better understand manufactured food microstructures other than simple observation, there is an avenue to improve transport models, safety, and process optimization. This work does not focus on the development of new software or simulations but on taking existing software available in other fields of research and applying it to published images of food products to show how it can be used to improve our understanding of food. The two example food systems are apple and rice. Using both foods, this work presents open source computational software to calculate intrinsic permeability using a lattice-Boltzmann simulation, pore-size distribution, pore connectivity using the Hoshen and Kopelman algorithm, and vapor diffusivity and tortuosity of water by a random-walk. Simulations are validated when available.

Keywords Permeability, tortuosity, pore-size, diffusivity, X-ray Microtomography

1. Introduction

Significant microstructural details are becoming available with newer imaging techniques such as X-ray micro-computed tomography (μCT). There remains, however, a great divide between availability of these structural details and the quantitative knowledge of transport properties that is commonly needed for food product and process design. While physics-based models of food processes can greatly improve their understanding and optimization, in order to realize the full potential of such models, transport properties are critical. As availability of experimentally measured properties is always severely limited and prediction models are generally empirical while also not considering food structure, an additional avenue of obtaining transport properties from microstructural information can be very rewarding.

Physics-based computational models in the literature are either overly simplistic to give a first approximation of a problem or can involve several governing equations that require many parameters. Examples of the latter models include frying (Halder et al., 2007a; Warning et al., 2012), bread baking (Zhang and Datta, 2006), meat cooking (Dhall and Datta, 2011), and microwave puffing (Rakesh and Datta, 2013). For this latter case of models, parameters are either unavailable in literature, unable to be determined experimentally, or too costly and time demanding to justify determining their value. For example, values of intrinsic permeability are scarce in literature for food (potato (Datta, 2006), beef (Harper, 1962), peach (Harper, 1962), pear (Ho et al., 2006), and apple (Feng et al., 2004; Harper, 1962)). Hence, a sensitivity analysis must be performed with estimated values (e.g., Halder et al. (2007b)). As more parameters in a model are estimated, the accuracy and precision of the model decreases, thereby reducing its efficacy.

Imaging, on the other hand, provides an in-depth look into the microstructure of food but mostly lacks meaningful quantitative data. Several food structures have been imaged with μCT, such as aerated dairy foods (van Dalen, 2003), food foams (Lim and Barigou, 2004), frozen foods (Mousavi et al., 2007), chocolate (Frisullo et al., 2010), vegetables (carrot, broccoli, mushroom) (van Dalen et al., 2013), cereal (van Dalen et al., 2007), crackers (van Dalen et al., 2007), herbs (van Dalen, 2003), rice (van Dalen, 2003; Mohorič et al., 2009; van den Doel et al., 2009), apple (Ho et al., 2013, 2011; Verboven et al., 2008; Mendoza et al., 2007, 2010), bacon (Said et al., 2007), corn (Takhar and Zhang, 2009) and bread (Lape et al., 2008; Falcone et al., 2005). For

example, Takhar and Zhang (2009) used μCT to generate a 3D image of corn, segregate the 3D structure into its representative parts, and then run a drying simulation on the corn model. Imaging also faces the problem of sometimes being difficult for food due to its complex structure and high moisture content. Therefore, it is important to extract as much information when imaging is possible.

Figure 1 shows a variety of comparisons between pore configurations where, in each case, one or more measured properties are the same but other properties might be completely different. In each comparison, the configuration with the green arrow has the greater value, the equal sign represents both configurations having equal values, and the red down arrow represents a low value of the two configurations. Figure 1 demonstrates that characterizing pore shape, connectivity, and their effect on transport properties requires more than measurement of one quantity. As such, any continuum level model developed must therefore incorporate the effects of all of these quantities, such as pore size and tortuosity through properties, otherwise important details are being overlooked. For example, when comparing 1a, both configurations have the same pore diameters, but diffusivity and permeability are different because the right configuration has a higher tortuosity (represented by a lower diffusivity). Figure 1b compares the effect of open (left) and isolated (right) pores. Or, in Figure 1c, the Kozeny-Carman equation is a function of porosity to calculate permeability, but both configurations have the same porosity and different intrinsic permeabilities. Figure 1d shows how, compared to open pores (left), blind pores (right) can be misleading when looking at the volume and surface area of the pores. These comparisons ultimately mean that the type of continuum model for mass, heat, or momentum applied to model a food system must be based on the type of pore configuration of the sample, which is only achieved by measuring various quantitative properties and not only one.

We present computational tools that can be used to enrich the quantitative information gained from imaging by estimating commonly understood transport properties. Availability of these properties would also greatly benefit physics-based computational models by removing the guesswork in model parameter values. We focus on two foods, apples and rice, as examples because of their differing pore structure. The foods examined are apple (Ho et al., 2013, 2011; Verboven et al., 2008; Mendoza et al., 2007, 2010), Typhoon heat treated raw rice, and heat treated parboiled rice (van den Doel et al., 2009; Mohorič et al., 2009; van Dalen, 2003). Details regarding imaging ma-

terials and methods can be found in the aforementioned papers about the apple and rice samples. Apples are a cellular structure which means the internal structure is similar to a packing of flexible spheres. Rice, on the other hand, is a low porous material in its natural state but, upon processing, becomes highly porous resembling a bubbly interior due to the stretching of the carbohydrate solid matrix. Therefore, while these two structures might have similar macroscopic properties (such as porosity or density), they will have significantly different transport.

2. Computational Theory

Here, the choice of representative element volume (REV), the domain over which computations are made, is introduced first. Computational algorithms for pore size distribution, diffusivity, tortuosity, and intrinsic permeability are discussed next.

2.1. Representative Element Volume (REV)

Figure 2 shows the underlying principle behind a representative element volume (REV). As the volume decreases below the continuum level, property values begin to fluctuate as the domain is no longer large enough to represent the entire system. One easy estimate of this limit is the average pore size of the porous food. Once the REV is approximately the size of the pores, the system becomes only pore and no solid. On the opposing end, as the volume begins to increase past another threshold value, material heterogeneity dominates and the property value changes. Reasons for these phenomena in food could be the core/seed region of a fruit, or the skin of a fruit or kernel, or simply the REV is larger than the product. Therefore, it is critical to use scans that are representative of the entire product in order to accurately calculate property information. In literature, several properties have been utilized (Okabe and Oseto, 2006; White et al., 2006; Costanza-Robinson et al., 2011; Li et al., 2009; Salama and Van Geel, 2008; Mendoza et al., 2007; Esveld et al., 2012a,b), primarily depending on the focus of the study, to determine the REV. For the purpose of this study, porosity and permeability will be examined as they are a measure of how porous the solid is and a measure of how connected the void space is, respectively.

2.2. Pore Size Calculation

The main reason for defining pores by their volume and surface area is that transport properties can be calculated from these two values (Nakashima and Kamiya, 2007; Bear, 1972; Hurlimann

et al., 1994). Examples of how the ratio of surface area to volume can be used to calculate permeability is presented later. Nakashima and Kamiya (2007) present the relationship between diffusivity and the ratio of surface area to volume, which is not used here. The two theoretical limits of the surface to volume ratio are given by Eq. 1, the lower limit, and Eq. 2, the upper limit where a is the dimension of a cubic CT voxel (3D image cubes). The lower limit is different from the volume to surface area ratio for a sphere by a factor of 1.5 because the spherical pore is discreet rather than smooth (Nakashima and Kamiya, 2007). Points below this line can be attributed to this factor. The upper limit comes from the assumption of a series of long rectangular prisms where the ends are ignored. A schematic of both is shown in Figure 3.

$$S = \lim_{V \to \infty} 6\pi \left(\frac{3V}{4\pi} \right)^{2/3} \tag{1}$$

$$S = \lim_{V \to \infty} \frac{4}{a} V \tag{2}$$

2.3. Vapor Diffusivity and Tortuosity

Tortuosity is a measure of the diffusive resistance of a molecule between free space and a porous media. In porous media, (vapor) diffusivity, $\mathbf{D}$, and tortuosity, τ, are not constant but tensors due to the anisotropy in the structure versus free space where transport proceeds unhindered. Therefore, when running a random-walk simulation, looking at the mean-square displacement in each direction at long times is necessary. An arbitrary example of a hindered random-walk in a porous structure is depicted in Figure 4. The mean square displacement in the jth direction is given by:

$$< x^j(\xi)^2 >= \frac{1}{n} \sum_{i=1}^{n} (x_i^j(\xi) - x_i^j(0))^2 \tag{3}$$

where n is the number of walkers and ξ is the dimensionless integer time. The dimensionless integer is the time to jump to the nearest pore voxel (there is six possibilities in a simple cubic lattice). If the walker encounters a solid voxel, the jump is not performed and the time increments by one (Nakashima and Kamiya, 2007). In free space, the mean-square displacement, $< r^2 >_{free}$, is given by:

$$< x^2 >_{free} = < y^2 >_{free} = < z^2 >_{free} = \frac{1}{3} < r^2 >_{free} = \frac{a^2 \xi}{3} \tag{4}$$

The tortuosity is then calculated by taking the dimensionless time derivative of Eq. 4 and dividing by Eq. 3. The tortuosity in the jth direction is then given by Eq. 5 at long times. Otherwise, the species will not interact with the solid part of the porous medium. One limitation is at infinity when the time derivative of the mean square displacement equals zero due to the pore not being infinitely open. This equation then applies up to the time at which the mean square displacement is no longer increasing. Figure 4 shows the gradual progression from free movement to restricted and, finally, to when the molecule is effectively trapped.

$$\tau^j = \frac{\frac{d < (x^j(\xi))^2 >_{free}}{d\xi}}{\frac{d < x^j(\xi)^2 >_{pore}}{d\xi}} = \frac{\frac{a^2}{3}}{\frac{d < x^j(\xi)^2 >_{pore}}{d\xi}} \text{ as } \xi \to \infty \tag{5}$$

There are two main definitions of tortuosity. The first definition is the tortuosity presented in Eq. 5 which is commonly employed in NMR diffusometry. The second is the square root of Eq. 5 and is used in some parts of literature. The diffusivity in the jth direction for long-times in the porous media, D_{pore}, for a non-sorbing species, that is then equal to:

$$D^j_{pore} = \frac{\frac{a^2}{3} D_{free}}{\tau^j} \tag{6}$$

where D_{free} is the free space diffusivity of any molecule. Later, D_{free} is assumed to be that of water vapor.

2.4. Intrinsic Permeability

Intrinsic permeability is a measure of the ability of a fluid to flow through a porous media. It is important in Darcy's law, a phenomenological equation (Eq. 7) that relates volumetric flux, q, to a pressure gradient, dP/ds. Pressure driven flow in food materials is relevant during such processes as microwave heating, frying, and intensive heating where phase change creates a pressure difference within the material. Pressure driven flow also occurs in extraction and capillary flow in unsaturated food (Datta, 2006).

$$q = \frac{k_{in}}{\mu} \frac{dP}{ds} \tag{7}$$

To calculate the intrinsic permeability of the samples, two approaches were considered. First, a fluid flow simulation using the lattice Boltzmann method was employed. A lattice Boltzmann simulation was used versus a discretized Navier-Stokes equation primarily because it is meshless. This reason is extremely important for complex geometries, like the ones from actual images, because the boundaries are not smooth which would make meshing extremely difficult and more computationally intensive. If the simulation did not work because the pores were not connected from end to end, then a least upper bound for the intrinsic permeability was estimated from traditional porous media theory based on the image resolution and pore size distribution.

2.4.1. Estimated Intrinsic Permeability

In order to calculate the intrinsic permeability, three approaches were considered: the Kozeny-Carman estimate (Hurlimann et al., 1994), the Kozeny-Carman equation (Bear, 1972), and the bundle of tubes equation (Eq. 8 (Bear, 1972)).

$$k_{in} = \frac{\pi n_t R^4}{24\tau} \tag{8}$$

The bundle of tubes model is the simplest and most well-known equation for determining permeability. It is based on assuming a collection of capillary tubes in a porous media and derivated from the Hagen-Poisseuille's law governing flow in a tube. Then, by also assuming only a third of the tubes go in each direction, a factor of $1/3$ reduces the permeability further. In the equation, n_t is the number of tubes per cross sectional area and R is the capillary radius. This equation relates to the previous two equations if the pores are considered circular because then the porosity is given by $\phi = n_t \pi R^2$ and Eq. 8 looks similar to the Kozeny-Carman equation:

$$k_{in} = \frac{\phi R^2}{24\tau} \tag{9}$$

For the purpose of estimating permeability in non-connected samples, the bundle of tubes model will be assumed. This assumption is based on the fact that the limiting transport is through the solid walls where the pores are smaller than what imaging can capture thereby ignoring the effect of large pores artificially increasing the permeability when transport is limited by the lack of pores being interconnected.

2.4.2. Simulated Intrinsic Permeability

To simulate fluid flow though the compiled images, the discrete lattice Boltzmann (LB) equation using a D3Q19-lattice and Bhatnagar-Gross-Krook (BGK) collision operator (single-time relaxation approximation) is used (Eq. 10). The discrete LB equation with the BGK operator is a computational fluid dynamics simulation using statistical mechanics that is equivalent to the Navier-Stokes equation (Shan and Chen, 1993):

$$f_i(\mathbf{x} + \mathbf{e}_i, t + 1) - f_i(\mathbf{x}, t) = \frac{1}{\gamma}[f_i^{eq}(\mathbf{x}, t) - f_i(\mathbf{x}, t)] \tag{10}$$

for $i = 0, 1, ..., 18$, where the lattice velocity vectors are $|\mathbf{e}_0| = 0$,$|\mathbf{e}_i| = 1$ for $i = 1...6$, and $|\mathbf{e}_i| = \sqrt{2}$ for $i = 7...18$. In Eq. 10, $f_i(\mathbf{x}, t)$ is the distribution function, $f_i^{eq}(\mathbf{x}, t)$ is the equilibrium distribution function and γ is the relaxation time. The right-hand side of Eq. 10 is the collision operator. In order to recover the Navier-Stokes equation, $f_i^{eq}(\mathbf{x}, t)$ is equal to:

$$f_i^{eq}(\rho, t) = \omega_i \rho \left\{ 1 + \frac{\mathbf{e}_i \cdot \mathbf{v}}{c_s^2} + \frac{(\mathbf{e}_i \cdot \mathbf{v})^2}{2c_s^4} - \frac{v^2}{2c_s^2} \right\} \tag{11}$$

with the lattice speed of sound, $c_s = \frac{1}{\sqrt{3}}$, and the lattice weights, ω, equal to $1/3$ for $i = 0$, $1/18$ for $i = 1, ..., 6$, and $1/36$ for $i = 7, ..., 18$.

The macroscopic fluid density, ρ, viscosity, μ, and fluid velocity, $\mathbf{v}$, are calculated from

$$\rho(\mathbf{x}, t) = \sum_i f_i(\mathbf{x}, t) \tag{12}$$

$$\mu(\mathbf{x}, t) = c_s^2 \rho(\mathbf{x}, t)(\tau - 0.5) \tag{13}$$

$$\mathbf{v}(\mathbf{x}, t) = \sum_i f_i(\mathbf{x}, t)\mathbf{e}_i / \rho(\mathbf{x}, t) \tag{14}$$

The boundary conditions are no-slip at the wall using the bounce-back method (Degruyter et al., 2010). The boundaries perpendicular to the direction of the flow were padded in order to avoid periodic boundary conditions (Degruyter et al., 2010). Combining Eqs. 10-14, the Navier-Stokes equation can be derived. Thus, by simulating the continuum fluid dynamics in the pores at steady-state, we can apply Darcy's equation (Eq. 15) and determine the intrinsic permeability of pores.

In the simulation, a pressure drop, δ, and dynamic viscosity, μ, are input. The average velocity is calculated in the simulation, and intrinsic permeability, k_{in}, is then calculated from lattice units to actual units by multiplying by a^2.

$$k_{in} = \frac{\mu v_{avg} L}{\delta P} a^2 \tag{15}$$

3. Methods

3.1. Software

The programs presented herein are open source but have not been applied to food materials. The first three programs, Itrimming.nb, Clabel.nb and Rwalk.nb are from the nuclear science field (Nakashima and Kamiya, 2007). The programs are freely available (`staff.aist.go.jp/nakashima.yoshito/progeng.htm`) and require Mathematica$^{(R)}$ version 5.2 or later. To use these Mathematica$^{(R)}$ programs, users create a few folders and input stacks of binary images which are then analyzed. The user only needs to input basic information about images such as dimensions and input parameters for random walk. The fourth program, Palabos, is an open source lattice-Boltzmann software for complex CFD physics (`www.palabos.org/download-ql`) and uses the tutorial for permeability in porous media (Degruyter et al., 2010). The code was independently validated versus the bundle of tubes model for intrinsic permeability and versus a Menger sponge, a fractal geometry (Cihan et al., 2009) (data not shown). To perform the permeability simulation, binary images are first compiled by a Matlab script provided with the software. Then, the user inputs the 3D image size, pressure drop, and viscosity and then the simulation is ready to run. Surface plots are output throughout the simulation and finally a permeability in lattice units is output. These programs were used in conjunction with ImageJ (Schneider et al., 2012) for conversion from greyscale to binary. In ImageJ, the *ImageJ 3D Viewer* plugin was used for generating 3D images.

3.2. Hardware

All simulations were run on a Dell Precision T3500 computer with 24 GB of RAM and a Intel(R) Xeon(R) CPU W3520 2.67 GHz processor. For the random walk simulations, a Windows 7 64 bit operating system and lattice Boltzmann simulations were run on an Ubuntu operating system. Simulation times were six hours for a random walk and 1.5 hours for a lattice Boltzmann simulation on a 1.38 mm^3 sample of an apple.

3.3. Image Thresholding

Before calculating property data, greyscale images of CT scans (Figure 5a) were converted into binary images. In order to do this, Itrimming.nb was used to determine a histogram of the greyscale for each 3D geometry. Itrimming.nb output a probability density function of voxel greyscale intensity. X-ray microtomography does not necessarily output pores (white) and solid (black) but outputs a significant amount of grey images which are either pore or solid. Therefore, some criterion for disceminating between the grey that is solid and the grey that is pore must be used because the images did not always demonstrate a clear bimodal distribution. Nakashima and Kamiya (2007) used the average pixel intensity of the bimodal distribution. As shown in Figure 5b, this technique could not be used. Instead, visual inspection with ImageJ (Figure 5c), followed by the operation 'despeckle', were used (Figure 5d). The 'despeckle' operation removes individual, isolated black and white spots that are noise. The images could then be compiled for greater visual analysis. Figures 6a and 6b show compiled images for the pores and solid matrix, respectively. A sensitivity of plus or minus 5 grey levels for thresholding was then analyzed to see the effect of the choice. Figures 7a and 7b show the effects of thresholding value on Typhoon heat treated raw and heat treated parboiled rice, respectively. Figures 7c-f show that the pore size distributions and transport properties do not change by orders of magnitude with variation in the threshold value, validating the method of visual inspection. An alternative method to visual inspection is the *Auto Threshold* plugin for ImageJ. The *Auto Threshold* plugin lets the user choose between 16 different thresholding techniques: Default (a varation of the IsoData algorithm), Huang (Huang and Wang, 1995), intermodes (Prewitt and Mendelsohn, 1966), IsoData (Ridler and Calvard, 1978), Li (Li and Tam, 1998), MaxEntropy (Kapur et al., 1985a), Mean (Glasbey, 1993), MinError(I) (Kittler and Illingworth, 1986), Minimum (Prewitt and Mendelsohn, 1966), Moments (Tsai, 1985), Otsu (Otsu, 1975), Percentile (Doyle, 1962), RenyiEntropy (Kapur et al., 1985b), Shanbhag (Shanbhag, 1994), Triangle (Zack et al., 1977), and Yen (Yen et al., 1995). No one method is 'correct', but a method can be 'wrong'. Visual inspection of the chosen thresholding technique, along with a sensitivity to the method, is the best, and safest, route in processing images.

3.4. Analysis of Pore Structure: Diameter, Connectivity, Porosity

Clabel.nb is a cluster-labeling program that finds all pore clusters and calculates their center of gravity, volume and surface area and whether they touch the outer edge of the geometry or

not. If the pore touches the outer edge of the image, the image edge is not considered part of the surface area. The ratio of volume to surface area is important as it represents an approximate pore diameter if the pores are considered spheres (Nakashima and Kamiya, 2007). Additionally, the program outputs porosity and relabeled 2D CT scans in order to visualize which pores are the largest. The program outputs the total number of solid voxels and knowing the total number of voxels in the set of images leads to the trivial calculation of porosity. These relabeled 2D images can be reconstructed into a 3D geometry using ImageJ as displayed in Figure 6a where the whiter the pore, the larger the volume. Pore voxels are considered connected if the faces touch while vertices and edges touching is treated as unconnected. To do the rapid calculation, the fast algorithm by Hoshen and Kopelman (1976) is employed. Nakashima and Kamiya (2007) discuss the algorithm in greater detail.

3.5. Vapor Diffusivity and Tortuosity

Rwalk.nb simulates a 3D random walk for a non-sorbing species only in the pore space (there is no transport through solid) on a simple cubic lattice to neighboring voxels that share faces. The program outputs the mean-square displacement, $\langle r^2 \rangle$, which can then be used to calculate tortuosity, τ, anisotropy in the x-y-z direction within the pore, as well as diffusivity, if the free space diffusivity is known. The random walk is carried out for a 'long time' such that the walker experiences the constriction of being within a porous material. For all simulations, 6×10^6 lattice time steps and 10000 walkers were used (computational limitations in memory prevented lengthier simulations). The square root of the number of steps is the average distance from the starting point. Based on the largest pore volume and assuming it to be a sphere, an approximate number of steps can be calculated such that the walker will see the solid matrix. As the random walk is carried out on a finite geometry and random walk might eventually lead to a walker leaving the domain, a mirror periodic boundary condition is used (see Nakashima and Kamiya (2007) for a schematic). Since at the boundary a mirror image of the plane is generated, the walker continues into the mirrored geometry.

3.6. Intrinsic Permeability

Palabos is an open-source CFD program that uses a lattice Boltzmann (LB) model to simulate fluid flow. The calculation of the intrinsic permeability follows the tutorial freely available on

the Palabos website as done by Degruyter et al. (2010). The pressure gradient between the inlet and outlet is entered along with the geometry size. Then, the average velocity is calculated and finally using Darcy's equation, the intrinsic permeability in one direction is calculated. In order to adhere to Darcy's equation, the pressure gradient is set low enough to make the inertial term approximately zero. Either the images can be resliced in ImageJ or the code can be rewritten to calculate flow in the other two directions in order to calculate the intrinsic permeability anisotropy in the x-y-z direction. The permeability is output in lattice units and can be easily converted to real units.

4. Results and Discussion

4.1. Representative Elemental Volume(REV)

Figures 8a-c show porosity versus REV size and Figures 8d-f and show the intrinsic permeability versus REV where the red points are intrinsic permeabilities calculated from the bundle of tubes model (Eq. 8). The porosities for Typhoon heat treated raw rice, heat treated parboiled rice, and apple were in the ranges of 0.1-0.58, 0.51-0.9, and 0.2-0.31 respectively. As expected, the porosity and permeability values become much more scattered at small REVs and more noticeable as the REV volume approaches the average pore volume of the material. For apple, Mendoza et al. (2007) calculated an REV size of 1.3 mm^3. The transport properties presented in Figures 8d-f for both Typhoon heat treated raw and heat treated parboiled rice show that as the REV size increases, the pores become disjoint but at small REVs, an intrinsic permeability can be measured. The right side of Figure 1d is an example of such a phenomena. On the small scale, connected pores are observed but as the scale increases, it becomes evident the pores are not connected across both types of rice. This observation illustrates why understanding the structure of the food is important to formulating transport models.

Unlike soils or rocks where the material is more like a packed-bed (which is always connected), food materials are more diverse. They can be a collection of cells (such as a fruit) and resemble a packed bed, be a foam at low porosity where the solid matrix is connected (such as bread or rice while the pores are still small), or be a foam at high porosity where the solid matrix is still connected but now the pores are large enough so that they have become connected (such as bread

at later stages of baking when it is very porous). Foods in the first case can be modeled much like soils. In the latter two cases, foods are essentially the inverses of soils in a sense, depending on the porosity and connectivity of the pores. Whereas soils are collections of particles to form a 'solid', foods are a solid with a collection of pores within them. Foods such as uncooked rice or uncooked bread start off as solids with very little porosity. During cooking, these foods are infused with gas from various sources (e.g. evaporation, etc.), creating a bubbly material where the majority of pores are not connected, thereby limiting transport. As the porosity increases, the connectivity can increase changing the dominating mechanism of transport. Packed beds of beads are always connected but foods may not necessarily always be. This observation is a generalization of soils and foods but should be considered when developing transport models for porous media.

4.2. Pore Characterization

An overly simplistic analysis of μCT scans is to look at the pore geometries. Figure 6b shows the solid matrix, in white, of heat treated parboiled rice. To look at the pores instead of the solid, Figure 6a shows the pores of apple where the more white the pore, the greater the volume. Some of the pores in Figure 6a percolate the interior apple while others are dead-ends. While these images provide a qualitative understanding of the geometry, computational models need quantitative data. As such, the pore volume to surface area ratios were calculated to give a greater understanding of the sample in question.

Figures 9-11 show the pore size distribution for both types of rice and apple, respectively. The pore distributions are presented three different ways to demonstrate that there is no unique one way to represent pore information. Quite likely, the most effective is to not define a 'diameter' but rather look at the more informative surface area and volume of the pores (Figures 9a-11a). The frequency plots of pore size distributions (Figures 9b-11b) clearly show this is not an effective measure of pores when compared to the other figures as they show that there are a lot of small pores, but more importantly, Figures 9a-11a and Figures 9c-11c show that there are many large pores that account for a majority of the volume. Figures 9c-11c show that when the pores are weighted by their volume fraction, pores with a large ratio but small volume are hidden with pores with a large volume and the same diameter. Therefore, it is best not to classify pores by some characteristic ratio but by their surface area and volume separately. Figures 9a-11a give the most detailed quantitative understanding of the pores because they not only show volume and surface

area, but also characterize the shape by the two limits. The surface area and volume ratio can be used to estimate several transport properties including intrinsic permeability, vapor diffusivity, tortuosity, and electrical conductivity (Hurlimann et al., 1994; Nakashima and Kamiya, 2007).

4.3. Vapor Diffusivity and Tortuosity

An example of the random walk in the three plane cross sections is shown in Figure 12 for apple tissue. The directional mean square displacement for both rice and apple are shown in Figures 13a-c, the calculated diffusivities are shown in Figures 13d-f and the calculated tortuosities are shown in Figures 13g-i. The mean square displacements and diffusivities show that apple and rice are anisotropic, differing by one to two orders of magnitude between directions. These results give leverage to the assumption diffusivity can be considered a scalar but for greater precision, anisotropy would need to be incorporated into the model. The anisotropy can be explained from Figures 8a-c and by looking at the spatial gradient in porosity. Figures 8a-c show that the materials have a high porosity and a wider variation at lower REV sizes. When looking at the spatial gradient in porosity (figures not shown), there are plateaus of high porosity followed by sporadic valleys of low porosity in each direction. Therefore, the anisotropy is from the different spatial porosity profiles. Samples with higher tortuosity in a direction had deeper valleys in porosity than samples with constant porosity and shallow valleys.

One point of interest is the difference between Typhoon heat treated raw rice (lower porosity) and heat treated parboiled rice (higher porosity) in terms of diffusivity. The higher porosity heat treated parboiled rice shows a lower diffusivity. The mean square displacement plot shows that both exhibit restricted diffusion at long times but the Typhoon heat treated raw rice encounters restricted diffusion first. Hence, the Typhoon heat treated raw rice is primarily moving in only two directions and increasing the mean square displacement faster which increases the diffusivity. This fact demonstrates two limitations of the simulation. The first is that a high number of small pores leads to many molecules beginning in them and hence minimizing the significance of the diffusivity and tortuosity measurement. The second limitation is the inability to 'walk' through the solid matrix. Both of these factors would need to be incorporated to further improve the accuracy of the simulation. But most importantly, the values are comparable to literature.

The diffusivity predicted here is molecular diffusivity for the gas phase only (i.e., in the pores) and not an effective diffusivity for the entire tissue where the solid phase will also have to be taken

into account. The effective diffusivity, as is typically reported from most experiments, could be estimated using series (Eq. 16), parallel (Eq. 17) or their combination models (which model will work is not known a-priori). As an example, for $D_v = 1.0 \times 10^{-5} m^2/s$ (vapor diffusivity including the tortuosity effect) and $D_l = 2.3 \times 10^{-9} m^2/s$ (self-diffusion coefficient of water (Yu and Gao, 2001)), $K^* = c_v/c_l = 0.01$ (partition coefficient of apple estimated from Kaymak-Ertekin and Gedik (2004)), and writing Fick's law in terms of effective diffusivity and concentration gradient in the liquid phase (i.e., the solid material that contains the liquid), one obtains $D_{eff} = 3.25 \times 10^{-9} m^2/s$ for series model (Eq. 16) which is one third of measured diffusivity ($D_{eff} = 1.01 \times 10^{-8} m^2/s$) from Ho et al. (2011). For a possible parallel arrangement (Eq. 17), $D_{eff} = 3.16 \times 10^{-8} m^2/s$, which is three times higher in value than that of the experiment from Ho et al. (2011). These results show that the measured experimental gas diffusivity data should be consistent with observed gas effective diffusivity.

$$\frac{1}{D_{eff,\perp}} = \frac{\phi}{D_v K^*} + \frac{1-\phi}{D_l} \tag{16}$$

$$D_{eff,\parallel} = \phi K^* D_v + (1-\phi) D_l \tag{17}$$

The size of the sample plays a major role in the type of measured or simulated transport as well. Small samples, relative to the largest pore volume, are more likely to have parallel transport but as the geometry scales larger, the pores will more likely become unconnected depending on the material. Smaller measured samples will have effective gas diffusivities (the same as pore gas diffusivity) whereas larger samples will be several orders of magnitude different between effective diffusivity and gas diffusivity.

Table 1 shows effective gas diffusivities in literature versus pore gas diffusivity calculated from this work. Diffusivities in table are for gas phase diffusivity. The table demonstrates that in porous media, the gas effective diffusivity is much lower than the vapor diffusivity because of the unconnected pores and transport between phases. Diffusivities several orders of magnitude below the calculated value in this work represent porous media where the microstructure is unconnected while gas effective diffusivities near the vapor diffusivity are of a microstructure that has connected pores leading to parallel transport, a conjecture of the microstructure is added to the values in Table 1.

The vapor diffusivity simulated for apple was 6.3×10^{-6} m^2/s while experiment lists 4.90×10^{-6}

m^2/s (Harper, 1962) and $6times10^{-7}$ m^2/s (Forbito et al., 1981). This comparison is in excellent agreement with both these experiments.

The diffusivity for Typhoon heat treated raw rice was approximately 2.0×10^{-6} m^2/s and for heat treated parboiled rice, was 5.0×10^{-6} m^2/s. These values are significantly higher than the reported values from experiments due to the aforementioned reasons.

The tortuosity in Typhoon heat treated raw rice is approximately 2.0 and in heat treated parboiled rice is 3.8. The tortuosity in apple is approximately 3.9. Experimentally reported tortuosity is 5.1 (Harper, 1962) and 33.3 (Forbito et al., 1981) for apples while there is no available experimental data for rice. Several works have reported tortuosity (and hence vapor diffusivity) is a function of porosity by some exponent (Millington and Quirk, 1961; Guo, 2012). One common relationship is $\tau(\phi) = \phi^{-p}$ (Bear, 1972; Dullien, 1991; Mota et al., 2001; Dias et al., 2006). Assuming $p = 0.5$ (Guo, 2012) and for a porosity ranging from 0.01 to 0.99, the tortuosity ranges from 1 to 10 which provides further validation for the calculations provided within this paper.

The values of vapor diffusivity and tortuosity can be applied to modeling the drying of materials at later stages or the early stages of rehydration when moisture within pores does not hinder transport. The pores must also be connected, otherwise the effective diffusivity will be lower from transport through the solid.

4.4. Intrinsic Permeability

Figure 8 shows the results for porosity and intrinsic permeability. The points in red in Figures 8d-f represent when the permeability was calculated from the bundle of tubes model (Eq. 8). The points in red in Figures 8a-c are the corresponding porosities. For the bundle of tubes model, one tube per cross sectional area with a tube diameter of 2 μm was assumed because the images had a resolution of approximately 5 μm meaning any pores must be smaller. As observed, the permeability became effectively zero at larger REV because pores were not connected. Hence, the bundles of tube model provides a least upper bound for permeability in rice. Current ongoing modeling work in rice puffing has shown that this value to be accurate in order to achieve the necessary pressure build-up within rice to cause puffing. For apple, the results are in excellent agreement with literature. Feng et al. (2004) report apple intrinsic permeabilities of 8.89×10^{-13} to 4.57×10^{-11} m^2 for a porosity of 0.33 to 0.77. Harper (1962) reports a value of 9.0×10^{-11} m^2 for freeze dried apple. Both of these results are much higher than the reported value for pear

cortex and vascular bundle samples of 2.35×10^{-19} and 4.51×10^{-17} m^2, respectively (Ho et al., 2006). The simulated and calculated intrinsic permeability values can be applied to modeling where pressure driven flow is important, such as rapid drying. These values can also be used as a measure of connectivity and ability for a material to puff due to the resistance of flow from pressure accumulation within the interior of the material.

5. Conclusion

A series of new computational methods for estimating transport properties for foods has been presented, thus increasing the quantitative understanding of food structures and transport models. By beginning with μCT scans of rice and apple, pore sizes, REV, tortuosity, diffusivity, and permeability have all been calculated without the need for complicated experimental set-ups. Calculated values were validated against experimental literature data when available. A new approach to pore size characterization was discussed along with the rational for treating pores not by a diameter but by their connectivity, volume and surface area. The basic algorithm of a random walk demonstrated the ease of finding the tortuosity and diffusivity of a material while the permeability calculation presented exhibited the importance of knowing a material's connectivity. With these additional methods available, researchers will be able to develop improved quantitative understanding of foods and develop more accurate transport models, which should lead to more efficient design of improved products and processes.

Table 1: Effective gas diffusivities in literature versus gas diffusivity from this work and conjectured microsctructure, based on understanding from this work

Food	Gas	Value (m^2/s)	Conjectured microsctructure
Apple, freeze dried[1]	H_2O	4.9×10^{-6}	Connected pores[†]
Apple[2]	H_2O	3.2×10^{-7}	Mix of connected and unconnected pores
Apple[3]	H_2O	6.0×10^{-7}	Mix of connected and unconnected pores[Ш]
Apple[4]	H_2O	4.33×10^{-12}	Unconnected pores[‡]
Apple[5]	H_2O	6.3×10^{-6}	This work
Apple[6]	O_2	1.01×10^{-8}	Mix of connected and unconnected pores
Pear[7]	O_2	1.11×10^{-9}	Unconnected pores
Pear[8]	H_2O	4.36×10^{-11}	Unconnected pores
Rice, parboiled[9]	H_2O	$1 - 10 \times 10^{-12}$	Unconnected pores
Rice, parboiled[10]	H_2O	2×10^{-10}	Unconnected pores
Rice, parboiled[11]	H_2O	2×10^{-11}	Unconnected pores
Rice, heat treated parboiled[12]	H_2O	5×10^{-6}	This work
Rice, typhoon heat treated raw[13]	H_2O	2×10^{-6}	This work

[1]Harper (1962);[2]Feng et al. (2000);[3]Forbito et al. (1981) ;[4]Veraverbeke et al. (2003) ;[5]This work;[6]Ho et al. (2011) ;[7] Ho et al. (2006) ;[8]Nguyen et al. (2006);[9]Bualuang et al. (2012) ;[10] Elbert et al. (2001) ;[11]Chandra and Singh (1984);[12]This work;[13]This work

[†]Primarily parallel transport (Eq. 17);[‡]Primarily series transport (Eq. 16);[Ш]Combination of parallel and series transport

Table 2: Nomenclature

Symbol	Definition
a	size of one voxel
c_s	lattice speed of sound, lattice length per lattice time
D, **D**	Diffusivity and diffusivity tensor, $m^2\ s^{-1}$
e	lattice vector, lattice length per lattice time
f	distribution function, particles per volume
k_{in}	intrinsic permeability, m^2
K^*	partition coefficient
L	length, m
n_t	number of tubes per area, m^{-2}
p	exponent factor
P	pressure, Pa
q	volumetric flux, $m^3\ m^{-2}\ s^{-1}$
r	radial coordinate, m
R	Radius, m
s	arbitrary direction coordinate, m
S	Surface area, m^2
t	time, s
T	Temperature, K
v,**v**	velocity magnitude,velocity vector, $m\ s^{-1}$
V	Volume, m^3
x=(x, y, z)	coordinate vector, vector coordinates, m
Greek Symbols	
τ, τ	tortuosity and tortuosity tensor $m^2\ m^{-2}$
ξ	dimensionless integer time
γ	dimensionless relaxation time
δ	difference,
ω	lattice weights
ρ	density, $kg\ m^{-3}$
μ	dynamic viscosity, Pa s
ϕ	porosity, $m^3\ m^{-3}$
Subscripts	
avg	average
eff	effective
$free$	in free space
i	arbitrary index
l	liquid
$pore$	in porous media
v	vapor
$\parallel$	parallel
$\perp$	perpendicular

Superscripts	
j	direction

List of Figures

List of Tables

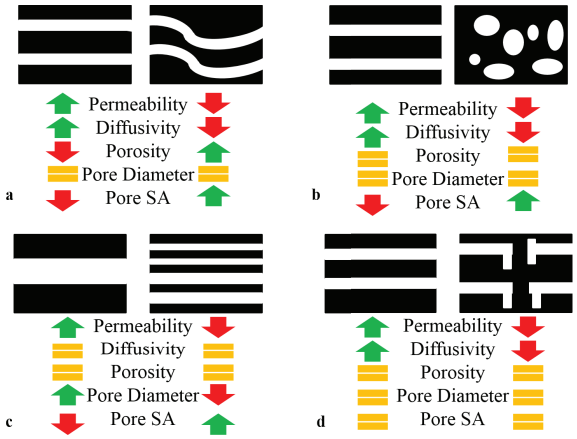

Figure 1: Various pore configurations showing how transport properties can depend on several measured properties. A) Shows tortuous pores lower transport; B) Isolated pores lower transport; C) Many small pores with the same porosity as a large pore have lower transport; D) Connectivity is required for transport. SA = surface area. Based on Nakashima and Kamiya (2007)

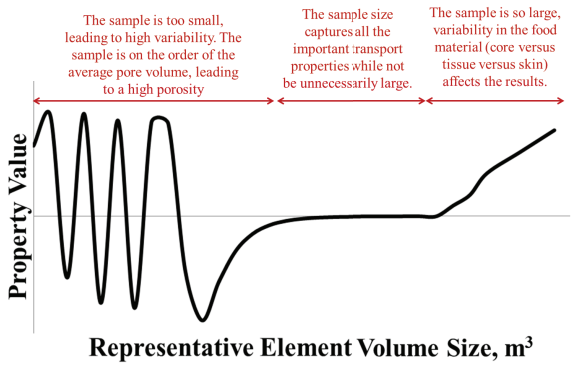

Figure 2: Arbitrary plot of a property versus sample volume. As volume increases, the calculated property will have a lower standard deviation and converge to a constant value. at this point, a representative element volume (REV) has been determined. A further increase in sample volume will ultimately reach a point in sample heterogeneity at the larger scales. Heterogeneities include the core of a fruit, the skin, or the sample size being larger than the product.

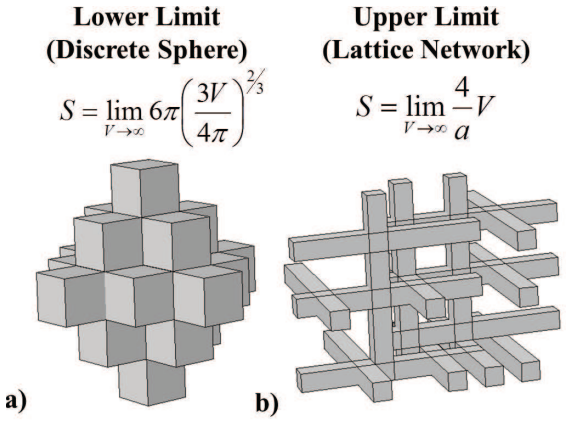

Figure 3: Example 3D pore structures for the theoretical lower (a) and upper limits (b) of the surface to volume ratio. a) A discrete, blocky spherical pore. b) a discrete interconnected lattice network. Based on Nakashima and Kamiya (2007)

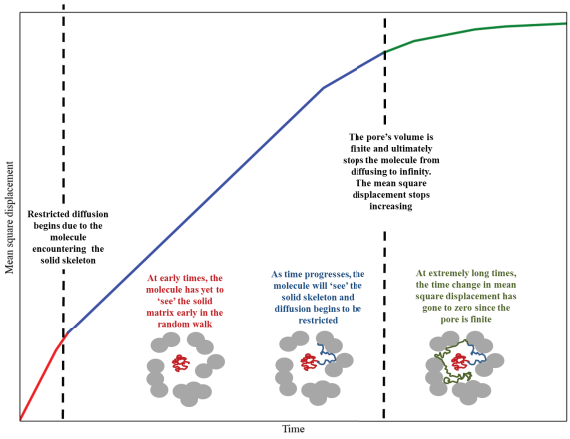

Figure 4: As time progresses in the random walk, the particle begins to experience restricted diffusion due to encountering the wall. All random walks in porous media must be run sufficiently long that the particle 'sees' the solid matrix. Based on Nakashima and Kamiya (2007)

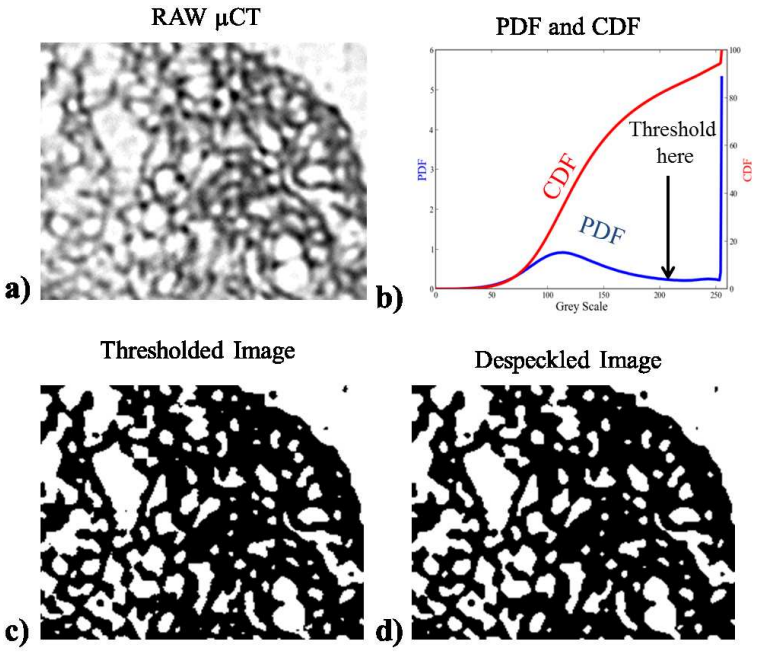

Figure 5: Thresholding procedure done on Typhoon heat treated raw rice. a) Grey scale images are taken with µCT. b) The probability distribution function (PDF) and cumulative distribution function (CDF). c) A threshold value is chosen in imageJ by visual inspection. d) The images are 'despeckled' to remove tiny white and black dots

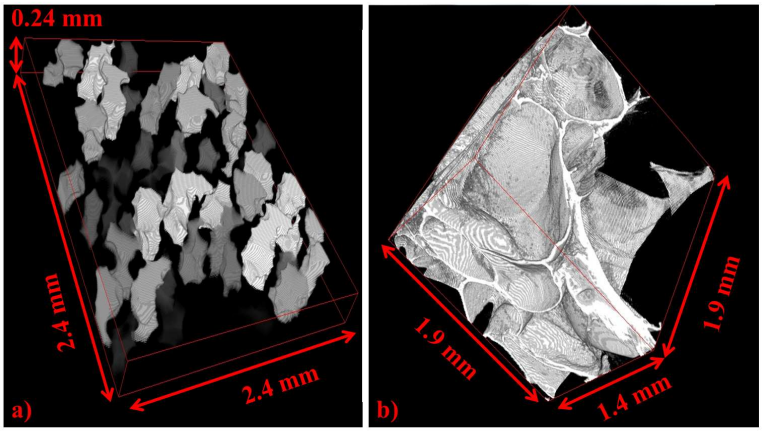

Figure 6: a) Labeled pores of apple. The whiter the pore the greater the volume. b) Solid matrix (white) of heat treated parboiled rice.

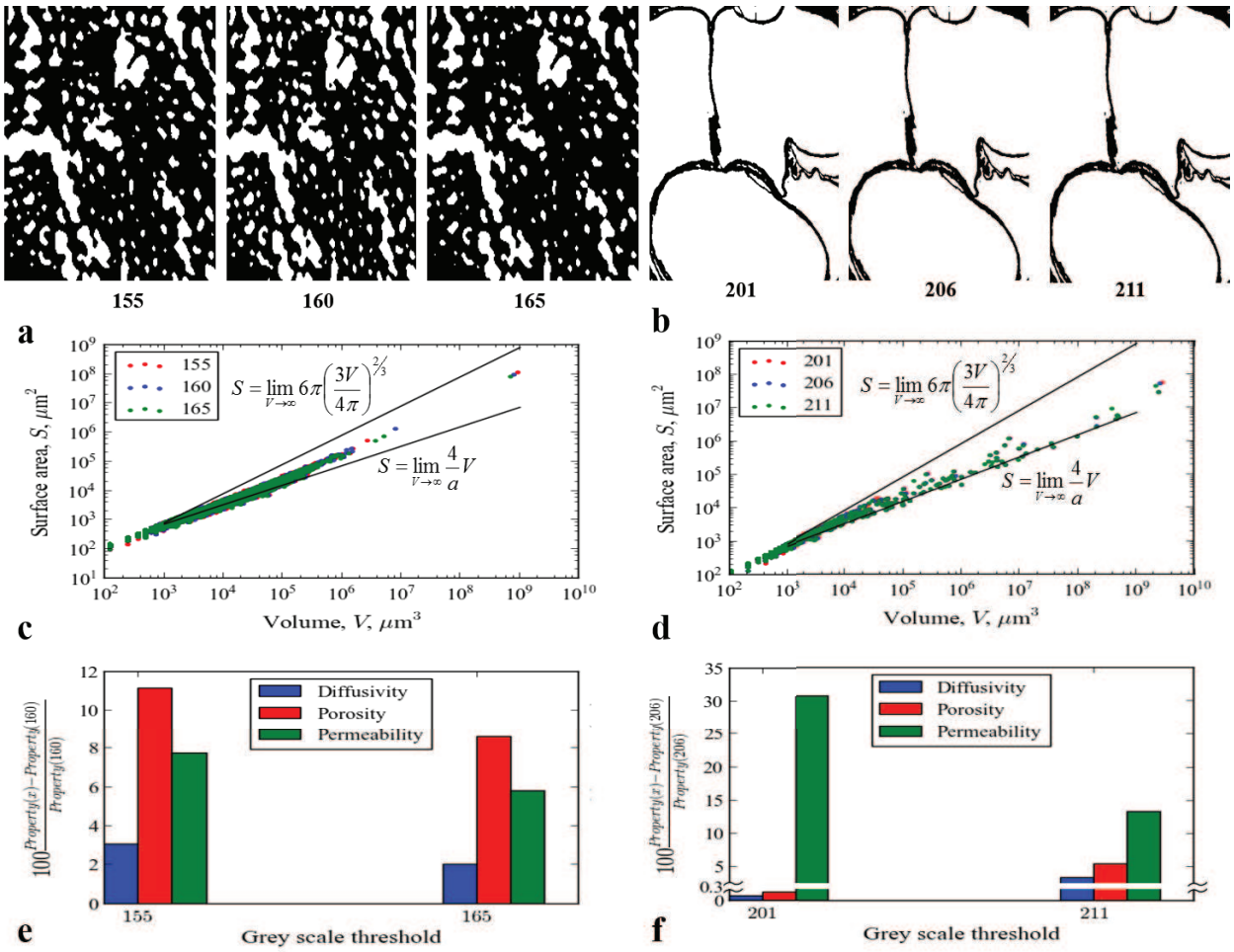

Figure 7: a) Three images thresholded differently for Typhoon heat treated raw rice; b) Three images thresholded differently for heat treated parboiled rice; c) Surface area versus volume for heat treated rice; d) Surface area versus volume for heat treated parboiled rice; e) Diffusivity, porosity, and permeability for heat treated rice; f) Diffusivity, porosity, and permeability for heat treated parboiled rice

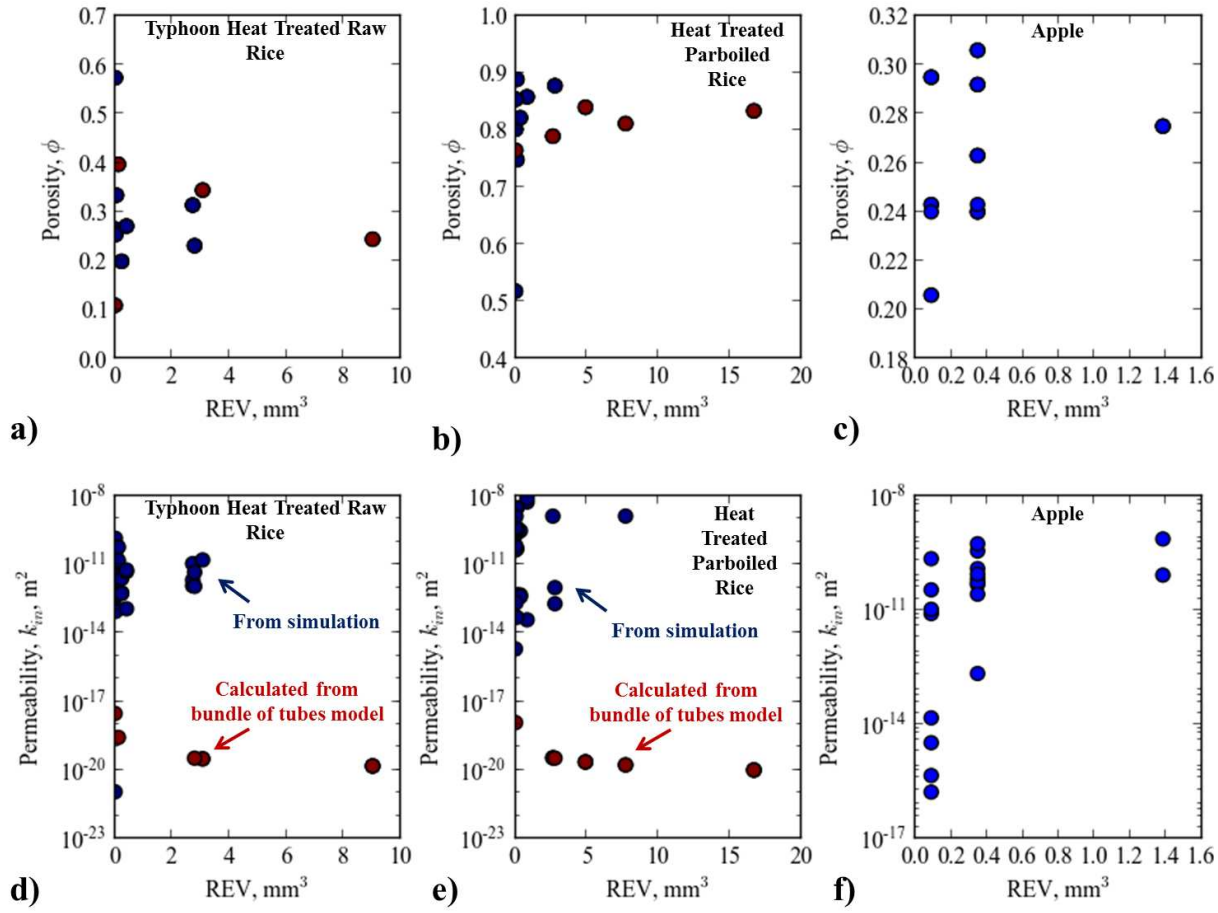

Figure 8: Porosity, ϕ versus REV size for a) Typhoon heat treated raw rice ,b) heat treated parboiled rice, and c) apple . Intrinsic permeability, k_{in}, versus REV size: d) Typhoon heat treated raw rice, e) heat treated parboiled rice, and f) apple. Red points represented a calculated intrinsic permeability from Eq. 8

. Blue points disappear at a higher REV, representing pores are no longer connected.

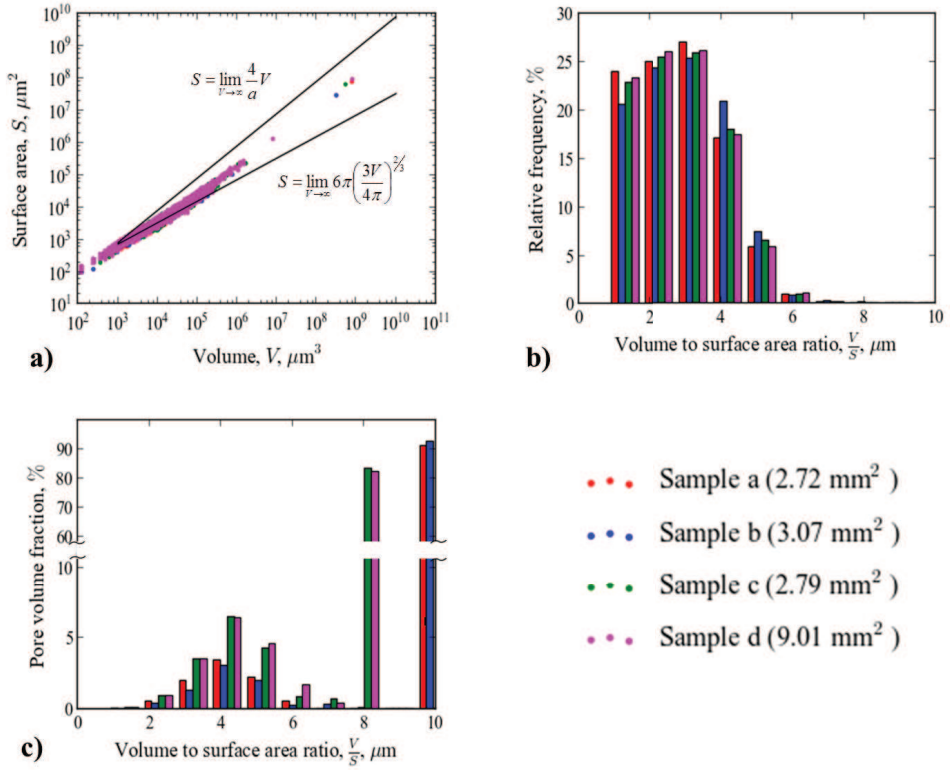

Figure 9: Typhoon heat treated raw rice analyzed for four samples a, b, c, and d of volumes 2.72, 3.07, 2.79, and 9.01 mm^3. a) Pore volume (V) versus surface area (S); b) relative frequency of pore volume to surface area (V/S); c) pore volume fraction

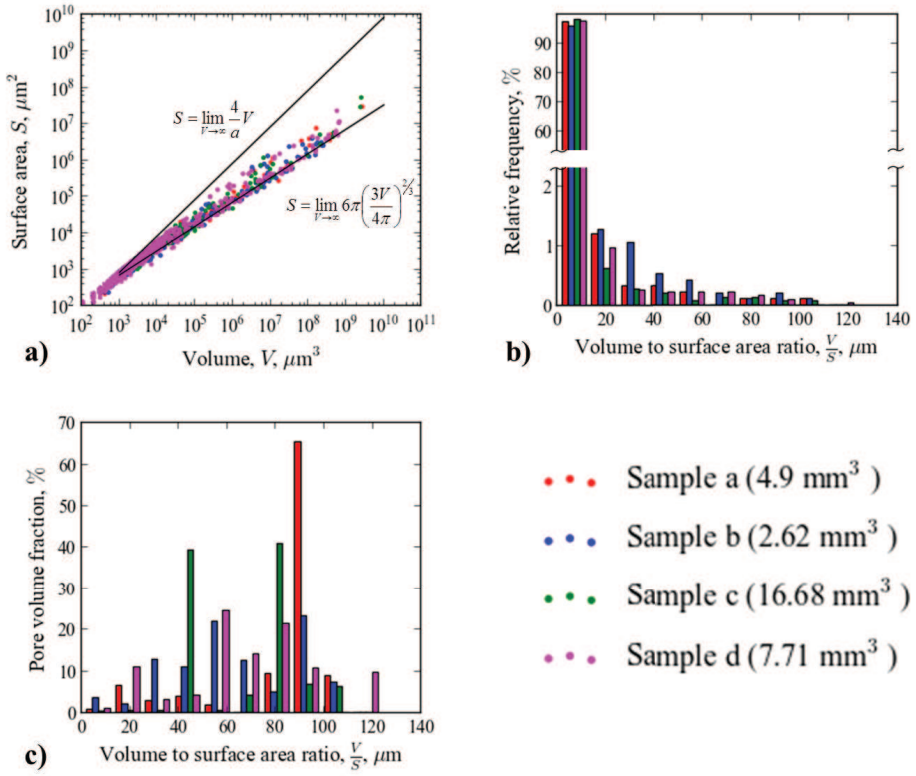

Figure 10: Four samples of heat treated parboiled rice. Sample a, b, c, and d are volumes 4.9, 2.62, 16.68, and 7.71 mm^3. a) Pore volume (V) versus surface area (S); b) relative frequency of pore volume to surface area (V/S); c) pore volume fraction

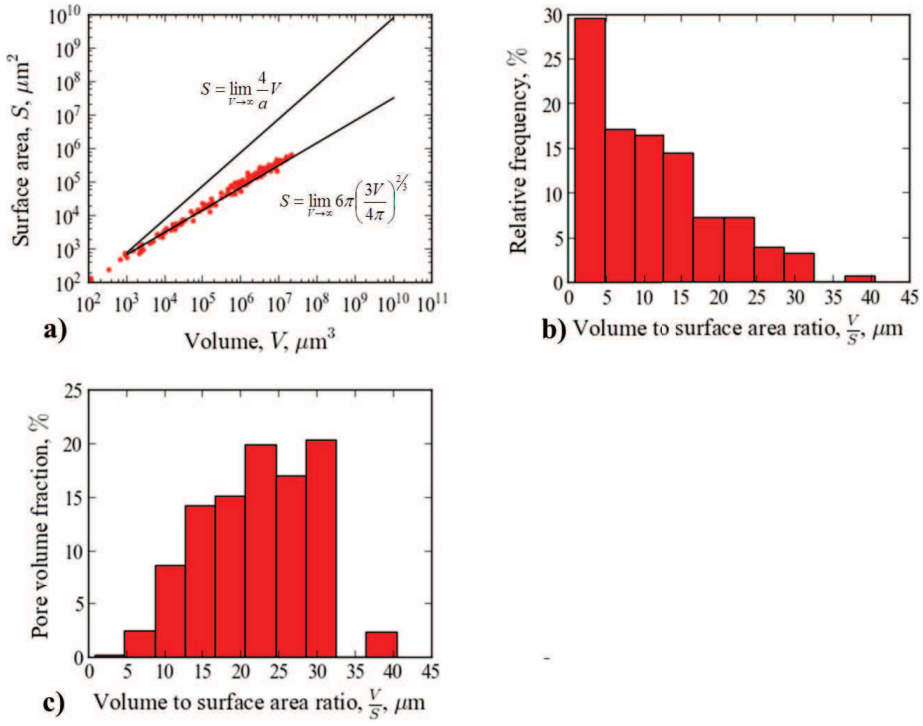

Figure 11: Apple pore size distribution at 1.38 mm^3 a) Pore volume (V) versus surface area (S); b)Relative frequency of pore volume to surface area (V/S); c) pore volume fraction

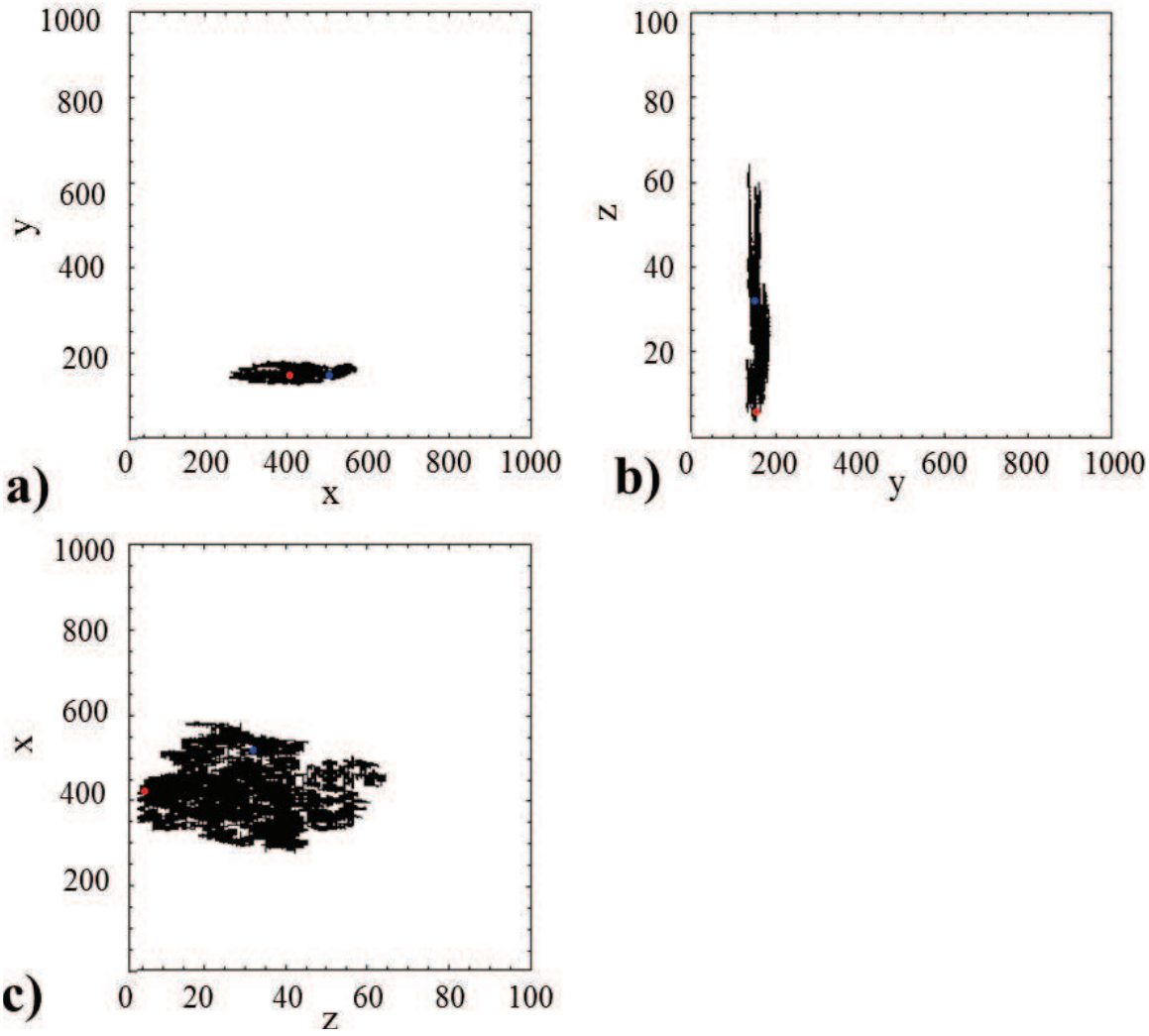

Figure 12: One example random walk in 1.38 mm^3 apple for 400000 time steps. a) x-y plane; b) y-z plane; c) x-z plane. The random walk is primarily in the x direction, demonstrating the restricted diffusion within a porous medium.

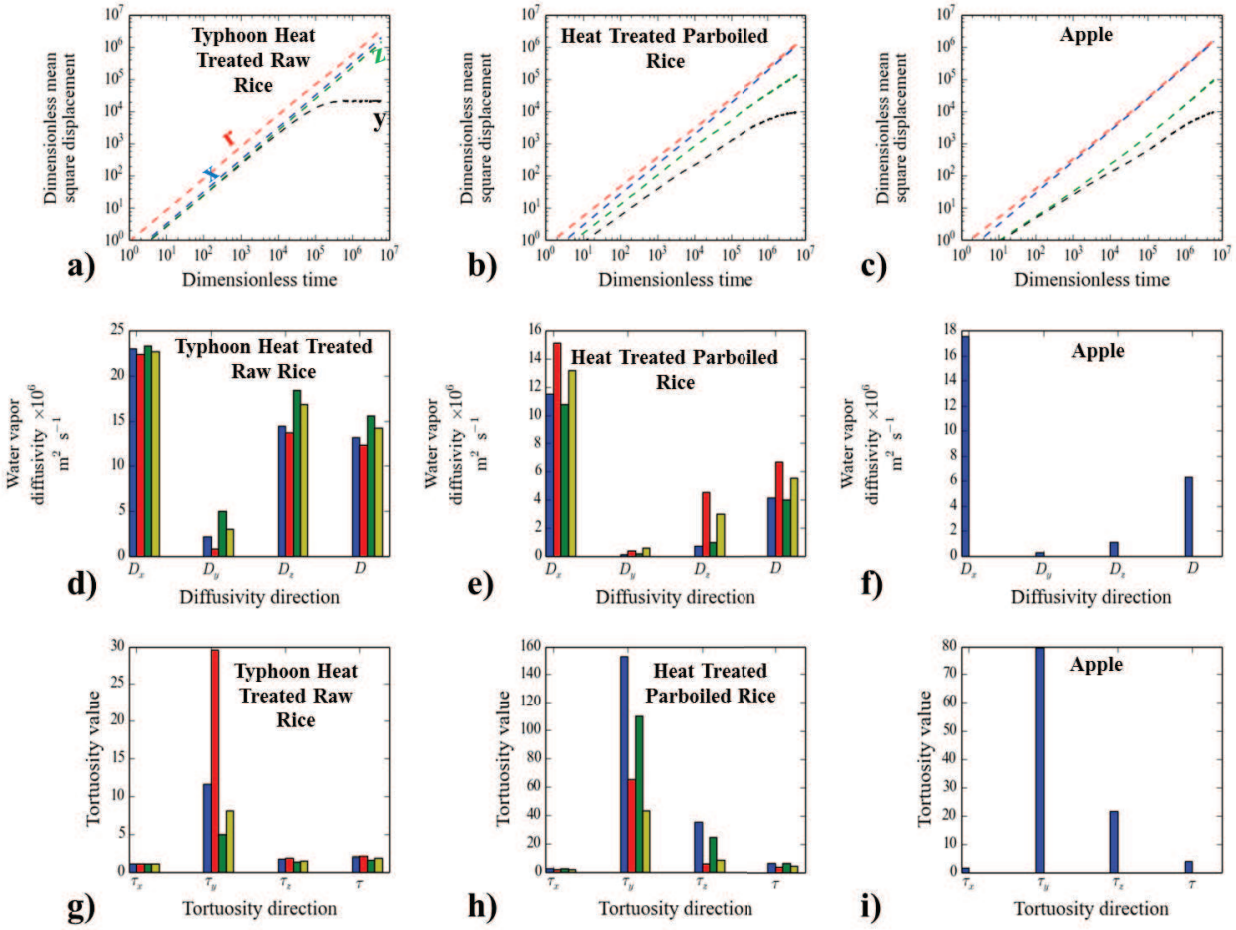

Figure 13: Directional mean square displacement for Typhoon heat treated raw rice (a), heat treated parboiled rice (b) and apple (c). Calculated directional diffusivity for Typhoon heat treated raww rice (all four aforementioned samples) (d), heat treated parboiled rice (all four aforementioned samples) (e) and apple (f). Calculated directional tortuosity for Typhoon heat treated raw rice (all four aforementioned samples) (g), heat treated parboiled rice (all four aforementioned samples) (h) and apple (i)

6. References

Bear, J., 1972. Dynamics of fluids in porous media. Courier Dover Publications.

Bualuang, O., Tirawanichakul, Y., Tirawanichakul, S., 2012. Comparative study between hot air and infrared drying of parboiled rice: Kinetics and qualities aspects. Journal of Food Processing and Preservation.

Chandra, P. K., Singh, R., 1984. Thin-layer drying of parboiled rice at elevated temperatures. Journal of Food Science 49 (3), 905–909.

Cihan, A., Sukop, M. C., Tyner, J. S., Perfect, E., Huang, H., 2009. Analytical predictions and lattice boltzmann simulations of intrinsic permeability for mass fractal porous media. Vadose Zone Journal 8 (1), 187–196.

Costanza-Robinson, M. S., Estabrook, B. D., Fouhey, D. F., 2011. Representative elementary volume estimation for porosity, moisture saturation, and air-water interfacial areas in unsaturated porous media: Data quality implications. Water Resources Research 47 (7), W07513.

Datta, A., 2006. Hydraulic permeability of food tissues. International Journal of Food Properties 9 (4), 767–780.

Degruyter, W., Burgisser, A., Bachmann, O., Malaspinas, O., 2010. Synchrotron x-ray microtomography and lattice boltzmann simulations of gas flow through volcanic pumices. Geosphere 6 (5), 470–481.
URL `http://geosphere.gsapubs.org/content/6/5/470.abstract`

Dhall, A., Datta, A. K., 2011. Transport in deformable food materials: A poromechanics approach. Chemical Engineering Science 66 (24), 6482–6497.

Dias, R., Teixeira, J. A., Mota, M., Yelshin, A., 2006. Tortuosity variation in a low density binary particulate bed. Separation and Purification Technology 51 (2), 180–184.

Doyle, W., 1962. Operations useful for similarity-invariant pattern recognition. Journal of the ACM (JACM) 9 (2), 259–267.

Dullien, F. A., 1991. Porous media: fluid transport and pore structure. Access Online via Elsevier.

Elbert, G., Tolaba, M. P., Aguerre, R. J., Suárez, C., 2001. A diffusion model with a moisture dependent diffusion coefficient for parboiled rice. Drying Technology 19 (1), 155–166.

Esveld, D., Van Der Sman, R., Van Dalen, G., Van Duynhoven, J., Meinders, M., 2012a. Effect of morphology on water sorption in cellular solid foods. part i: Pore scale network model. Journal of Food Engineering 109 (2), 301–310.

Esveld, D., van der Sman, R., Witek, M., Windt, C., van As, H., van Duynhoven, J., Meinders, M., 2012b. Effect of morphology on water sorption in cellular solid foods. part ii: Sorption in cereal crackers. Journal of Food Engineering 109 (2), 311–320.

Falcone, P. M., Baiano, A., Zanini, F., Mancini, L., Tromba, G., Dreossi, D., Montanari, F., Scuor, N., Nobile, M. A. D., 2005. Three-dimensional quantitative analysis of bread crumb by x-ray microtomography. Journal of Food Science 70 (4), E265–E272.

Feng, H., Tang, J., John Dixon-Warren, S., 2000. Determination of moisture diffusivity of red delicious apple tissues by thermogravimetric analysis. Drying technology 18 (6), 1183–1199.

Feng, H., Tang, J., Plumb, O., Cavalieri, R., 2004. Intrinsic and relative permeability for flow of humid air in unsaturated apple tissues. Journal of food engineering 62 (2), 185–192.

Forbito, P., Urbicain, M., Rotstein, E., 1981. Water vaporair effective diffusivity in apple tissues. Journal of Food Science 46 (6), 1960–1961.

Frisullo, P., Licciardello, F., Muratore, G., Del Nobile, M. A., 2010. Microstructural characterization of multiphase chocolate using x-ray microtomography. Journal of food science 75 (7), E469–E476.

Glasbey, C. A., 1993. An analysis of histogram-based thresholding algorithms. CVGIP: Graphical models and image processing 55 (6), 532–537.

Guo, P., 2012. Dependency of tortuosity and permeability of porous media on directional distribution of pore voids. Transport in Porous Media 95 (2), 285–303.

Halder, A., Dhall, A., Datta, A., 2007a. An improved, easily implementable, porous media based model for deep-fat frying: Part i: Model development and input parameters. Food and Bioproducts Processing 85 (3), 209 – 219.
URL `http://www.sciencedirect.com/science/article/pii/S0960308507705989`

Halder, A., Dhall, A., Datta, A., 2007b. An improved, easily implementable, porous media based model for deep-fat frying: Part ii: Results, validation and sensitivity analysis. Food and Bioproducts Processing 85 (3), 220–230.

Harper, J. C., 1962. Transport properties of gases in porous media at reduced pressures with reference to freeze-drying. AIChE Journal 8 (3), 298–302.

Ho, Q. T., Verboven, P., Fanta, S. W., Abera, M. K., Retta, M. A., Herremans, E., Defraeye, T., Nicolaï, B. M., 2013. A multiphase pore scale network model of gas exchange in apple fruit. Food and Bioprocess Technology, 1–14.

Ho, Q. T., Verboven, P., Verlinden, B. E., Herremans, E., Wevers, M., Carmeliet, J., Nicolaï, B. M., 2011. A three-dimensional multiscale model for gas exchange in fruit. Plant physiology 155 (3), 1158–1168.

Ho, Q. T., Verlinden, B. E., Verboven, P., Vandewalle, S., Nicolaï, B. M., 2006. A permeation–diffusion–reaction model of gas transport in cellular tissue of plant materials. Journal of experimental botany 57 (15), 4215–4224.

Hoshen, J., Kopelman, R., 1976. Percolation and cluster distribution. i. cluster multiple labeling technique and critical concentration algorithm. Physical Review B 14 (8), 3438.

Huang, L.-K., Wang, M.-J. J., 1995. Image thresholding by minimizing the measures of fuzziness. Pattern recognition 28 (1), 41–51.

Hurlimann, M., Helmer, K. G., Latour, L., Sotak, C. H., 1994. Restricted diffusion in sedimentary rocks. determination of surface-area-to-volume ratio and surface relaxivity. Journal of Magnetic Resonance, Series A 111 (2), 169–178.

Kapur, J., Sahoo, P. K., Wong, A., 1985a. A new method for gray-level picture thresholding using the entropy of the histogram. Computer vision, graphics, and image processing 29 (3), 273–285.

Kapur, J., Sahoo, P. K., Wong, A., 1985b. A new method for gray-level picture thresholding using the entropy of the histogram. Computer vision, graphics, and image processing 29 (3), 273–285.

Kaymak-Ertekin, F., Gedik, A., 2004. Sorption isotherms and isosteric heat of sorption for grapes, apricots, apples and potatoes. LWT-Food Science and Technology 37 (4), 429–438.

Kittler, J., Illingworth, J., 1986. Minimum error thresholding. Pattern recognition 19 (1), 41–47.

Lape, A., Jensen, S., Jeor, V. S., Lendon, C., 2008. Use of x-ray micro computed tomography in the evaluation of bread crumb structure. Microscopy and Microanalysis 14 (S2), 700–701.

Li, C., Tam, P. K.-S., 1998. An iterative algorithm for minimum cross entropy thresholding. Pattern Recognition Letters 19 (8), 771–776.

Li, J., Zhang, L., Wang, Y., Fredlund, D., 2009. Permeability tensor and representative elementary volume of saturated cracked soil. Canadian Geotechnical Journal 46 (8), 928–942.

Lim, K., Barigou, M., 2004. X-ray micro-computed tomography of cellular food products. Food research international 37 (10), 1001–1012.

Mendoza, F., Verboven, P., Ho, Q. T., Kerckhofs, G., Wevers, M., Nicolaï, B., 2010. Multifractal properties of pore-size distribution in apple tissue using x-ray imaging. Journal of Food Engineering 99 (2), 206–215.

Mendoza, F., Verboven, P., Mebatsion, H. K., Kerckhofs, G., Wevers, M., Nicolaï, B., 2007. Three-dimensional pore space quantification of apple tissue using x-ray computed microtomography. Planta 226 (3), 559–570.

Millington, R., Quirk, J., 1961. Permeability of porous solids. Transactions of the Faraday Society 57, 1200–1207.

Mohorič, A., Vergeldt, F., Gerkema, E., Dalen, G. v., Doel, L. v. d., Vliet, L. v., As, H. V., Duynhoven, J. v., 2009. The effect of rice kernel microstructure on cooking behaviour: A combined μ-ct and mri study. Food Chemistry 115 (4), 1491–1499.

Mota, M., Teixeira, J., Bowen, W. R., Yelshin, A., 2001. Binary spherical particle mixed beds: porosity and permeability relationship measurement.

Mousavi, R., Miri, T., Cox, P. W., Fryer, P. J., 2007. Imaging food freezing using x-ray microtomography. International journal of food science & technology 42 (6), 714–727.

Nakashima, Y., Kamiya, S., 2007. Mathematica programs for the analysis of three-dimensional pore connectivity and anisotropic tortuosity of porous rocks using x-ray computed tomography image data. Journal of Nuclear Science and Technology 44 (9), 1233–1247.

Nguyen, T. A., Verboven, P., Scheerlinck, N., Vandewalle, S., Nicolaï, B. M., 2006. Estimation of effective diffusivity of pear tissue and cuticle by means of a numerical water diffusion model. Journal of Food Engineering 72 (1), 63–72.

Okabe, H., Oseto, K., 2006. Pore-scale heterogeneity assessed by the lattice-boltzmann method. In: Proceedings of the international symposium of the society of core analysts, Trondheim, Norway.(SCA 2006-44).

Otsu, N., 1975. A threshold selection method from gray-level histograms. Automatica 11 (285-296), 23–27.

Prewitt, J., Mendelsohn, M. L., 1966. The analysis of cell images*. Annals of the New York Academy of Sciences 128 (3), 1035–1053.

Rakesh, V., Datta, A. K., 2013. Transport in deformable hygroscopic porous media during microwave puffing. AIChE Journal 59 (1), 33–45.

Ridler, T., Calvard, S., 1978. Picture thresholding using an iterative selection method. IEEE transactions on Systems, Man and Cybernetics 8 (8), 630–632.

Said, R., Schüller, R., Young, P., Aastveit, A., Egelandsdal, B., 2007. Simulation of salt diffusion in a pork (bacon) side using 3d imaging.
Salama, A., Van Geel, P. J., 2008. Flow and solute transport in saturated porous media: 1. the continuum hypothesis. Journal of Porous Media 11 (4).
Schneider, C. A., Rasband, W. S., Eliceiri, K. W., 2012. Nih image to imagej: 25 years of image analysis. Nat Methods 9 (7), 671–675.
Shan, X., Chen, H., 1993. Lattice boltzmann model for simulating flows with multiple phases and components. Physical Review E 47 (3), 1815.
Shanbhag, A. G., 1994. Utilization of information measure as a means of image thresholding. CVGIP: Graphical Models and Image Processing 56 (5), 414–419.
Takhar, P. S., Zhang, S., 2009. Drying of corn kernels: From experimental images to multiscale multiphysics modeling. In: Comsol Conference Proceeding 2009.
Tsai, W.-H., 1985. Moment-preserving thresolding: A new approach. Computer Vision, Graphics, and Image Processing 29 (3), 377–393.
van Dalen, G, B. H. A. H. H. C., 2003. 3-d imaging of foods using x-ray microtomography. GIT Imaging and microscopy 3, 18–21.
van Dalen, G., Koster, M., Nijsse, J., Boller, E., van Duynhoven, J., 2013. 3d imaging of freeze-dried vegetables using x-ray microtomography. In: Proceedings of the Micro-CT user meeting SkyScan, Hasselt, Belgium.
van Dalen, G., Nootenboom, P., Van Vliet, L. J., et al., 2007. 3d imaging and analysis of porous cereal products using x-ray microtomography.
van den Doel, L., Mohoric, A., Vergeldt, F., van Duynhoven, J., Blonk, H., van Dalen, G., Van As, H., van Vliet, L. J., 2009. Mathematical modeling of water uptake through diffusion in 3d inhomogeneous swelling substrates. AIChE Journal 55 (7), 1834–1848.
Veraverbeke, E. A., Verboven, P., Scheerlinck, N., Nicolaï, B. M., B. M., 2003. Determination of the diffusion coefficient of tissue, cuticle, cutin and wax of apple. Journal of Food Engineering 58 (3), 285–294.
Verboven, P., Kerckhofs, G., Mebatsion, H. K., Ho, Q. T., Temst, K., Wevers, M., Cloetens, P., Nicolaï, B. M., 2008. Three-dimensional gas exchange pathways in pome fruit characterized by synchrotron x-ray computed tomography. Plant Physiology 147 (2), 518–527.
Warning, A., Dhall, A., Mitrea, D., Datta, A. K., 2012. Porous media based model for deep-fat vacuum frying potato chips. Journal of Food Engineering 110 (3), 428–440.
White, J. A., Borja, R. I., Fredrich, J. T., 2006. Calculating the effective permeability of sandstone with multiscale lattice boltzmann/finite element simulations. Acta Geotechnica 1 (4), 195–209.
Yen, J.-C., Chang, F.-J., Chang, S., 1995. A new criterion for automatic multilevel thresholding. Image Processing, IEEE Transactions on 4 (3), 370–378.
Yu, Y.-X., Gao, G.-H., 2001. Study on self-diffusion in water, alcohols and hydrogen fluoride by the statistical associating fluid theory. Fluid phase equilibria 179 (1), 165–179.
Zack, G., Rogers, W., Latt, S., 1977. Automatic measurement of sister chromatid exchange frequency. Journal of Histochemistry & Cytochemistry 25 (7), 741–753.
Zhang, J., Datta, A., 2006. Mathematical modeling of bread baking process. Journal of Food Engineering 75 (1), 78–89.